Yang, Q., Danaie, M., Young, N., Broadley, V., Joyce, D. E., Martin, T. L., Marceau, E., Moody, M. P., & Bagot, P. A. J. (2019). Atom probe tomography of Au-Cu bimetallic nanoparticles synthesized by inert gas condensation. *Journal of Physical Chemistry C*, *123*, 26481-26489. https://doi.org/10.1021/acs.jpcc.9b09340

Atom Probe Tomography of Au-Cu Bimetallic Nanoparticles Synthesized by Inert Gas Condensation

Q. Yang[1,*] , M. Danaie[2], N. Young[1], V. Broadley[3], D. E. Joyce[3], T. L. Martin[4], E. Marceau[5], M.P. Moody[1], and P.A.J. Bagot[1]

1*Department of Materials, University of Oxford, Oxford, OX1 3PH, United Kingdom*

2*ePSIC, Diamond Light Source, Didcot, Oxford, United Kingdom*

3*Mantis Deposition Ltd., Thame, Oxfordshire, OX9 3RR, United Kingdom*

4*HH Wills Physics Laboratory, University of Bristol, Bristol, BS8 1TL, United Kingdom*

5*Univ. Lille, CNRS, Centrale Lille, ENSCL, Univ. Artois, UMR 8181 - UCCS - Unité de Catalyse et Chimie du Solide, F-59000 Lille, France*

E-mail: qifeng.yang@materials.ox.ac.uk

Abstract

The Inert Gas Condensation method (IGC) produces multimetallic nanoparticles in a metastable state that may exhibit heterogeneities of size, structure and composition. The deposition of IGC-fabricated nanoparticles on substrates allows for a detailed characterization by combination of aberration-corrected transmission electron microscopy (TEM) and Atom Probe Tomography (APT). Multiple particle monitoring and high-resolution TEM give access to the size distribution of Au-Cu nanoparticles (<10nm in diameter, bimodal distribution). TEM and APT show that the alloying between Cu and Au may stabilize the Ih structure for smaller particles (<4nm). Combining HR-STEM/EDX and 3D composition analysis by APT reveals that an excess of Cu may be present in a shell around the larger particles (>7nm), while Cu is more randomly distributed in smaller particles.

TOC Graphic

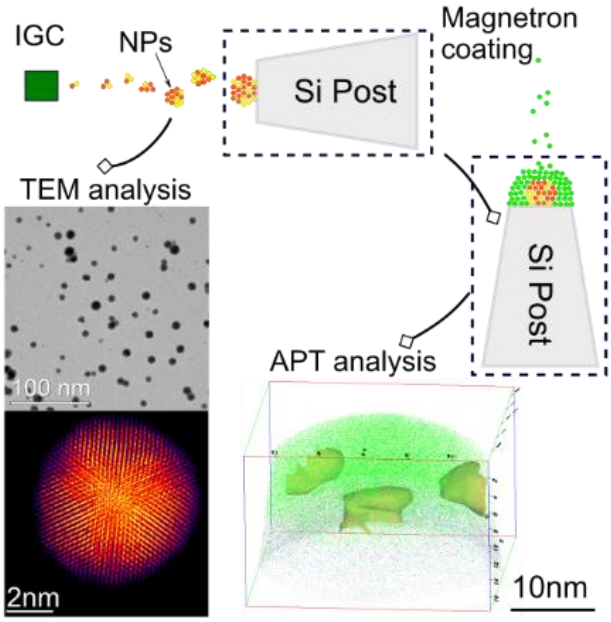

Introduction

Inert Gas Condensation (IGC) is a technique based on magnetron plasma sputtering and in-line mass filtering that allows deposition of metallic clusters and nanoparticles onto a variety of substrates, without constraints of nucleation and growth.[1,2] IGC has been reported to provide the unique ability to control the size,[2–5] composition[6], and even crystallographic structure[2] of metallic particles. Bimetallic particles have been prepared via this technique using either alloyed target or a combination of monometallic targets, and the formation of core-shell or Janus nanoparticles has been described, in particular when the metals are introduced sequentially.[4,5,7–15]

However, when the metals are introduced simultaneously, multi-metallic particles may be formed in out-of-equilibrium conditions, leading to metastable systems in which the homogeneity of the particles in terms of size, structure and distribution of the metals can be questioned. High Resolution Scanning Transmission Electron Microscopy (HR-STEM) in combination with EDX and EELS mapping is invaluable to reveal any segregated structures and to draw composition profiles across those individual particles. But the difficulty with such techniques is to determine the exact 3D atomic-scale distribution of the elements within the nanoparticles. TEM tomography has been used to characterize multimetallic nanoparticles, through the conversion of a series of 2D images into 3D reconstructions.[16,17] Nevertheless, difficulties exist for particles with complex geometries, electron beam damages, poor Z-contrast between elements, low Z elements and sample thickness.

In contrast, Atom Probe Tomography (APT) can theoretically address these difficulties, owing to its unique combination of 3D characterization with very high mass sensitivity (ppm).[18] As the composition measurement in APT relies on a time-of-flight mass spectrum, equally sensitive to all species, both light and heavy elements can be easily distinguished. APT is thus a potentially powerful technique to investigate metastable nanoparticles. However, there is only limited work associating APT and nanoparticle research. Initial attempts at capturing nanoparticles in an APT specimen needle used electrophoresis[19,20] providing crucial information about the distribution and embedding of elements in individual particles.[21] But a

major difficulty for analysis lies in distorted reconstructions, due to the rough surface morphology of such samples and to associated chaotic local field effects created by surface protutions.[22] Encapsulation of nanoparticles deposited on a flat substrate and FIB lift-out allowed improving the data quality, but have been implemented so far in a few instances only.[23–27]

In this study, we show that IGC is actually an efficient method for the manufacturing of identical nanoparticle-containing specimens intended for HR-STEM/EDX and APT analyses. While HR-STEM/EDX provides detailed information both on the size and structure of the nanoparticles, APT can reveal the 3D distribution of the atoms within. A complete characterization of the IGC-fabricated metastable bimetallic nanoparticles can be achieved, and possible heterogeneities can be evidenced. Au-based nanoparticles have been selected to validate this approach as a proof-of-concept.

Experimental

Particle fabrication

To fabricate the nanoparticles, the IGC method was carried out using a Mantis deposition NanoGen TRIO, which incorporates up to three separate targets in one IGC source, enabling the generation of elemental, bimetallic or trimetallic nanoparticles. In this experiment, Au (99.99% Scotech) and Cu targets (C103, 99.95%, Columbia Metals) were selected. These metallic targets were evaporated through magnetron sputtering under ionized Ar gas. The composition of the mixed ion gas formed was controlled by the DC power input applied to each target. The metallic vapor produced was condensed back into particles through a narrowing flight path, which increases the localized pressure and in turn increases the probability of collisions and subsequent nanoparticle formation. A more detailed description of the IGC method has been previously published.[27] For the present samples, a sputtering current of 60 mA was applied for Cu and Au targets, for a deposition time of 4.5 minutes in an argon flow of 60 sccm. Samples for both TEM and APT were produced during the same IGC run, which

allowed obtaining complementary characterization data from the two techniques. Deposition was carried out onto standard arrays of Si 2 μm flat-top posts (Cameca) for APT analysis. A holey carbon film-coated Cu grid (Agar Scientific) and a silicon nitride film grid were used as supports for bright-field TEM imaging, and for HR-STEM/EDX analysis, respectively. In order to avoid potential nanoparticle agglomeration, the deposition conditions were initially calibrated by quartz crystal microbalance (QCM) supplied by Inficon Cool Drawer. The number of particles deposited per second was evaluated from the QCM reading (ng/s), assuming that the density would correspond to that of an AuCu alloy (14.11g/cm^3) and that the particle size would be close to 10 nm. A calculation based on the beam area (50 mm diameter) led to an appropriate deposition rate of 2.4-3 ng/s for a sub-monolayer coverage. To measure the particle size, an in-line Meso-Q^{TM} quadrupole mass filter was used to monitor the overall size distribution of as-fabricated nanoparticles after gas condensation, without imposing a cut-off limit to the masses of the transiting charged particles.[3,27,28]

TEM

TEM analyses were conducted with various purposes, utilizing three instruments: a JEOL 3000F for bright-field imaging used for particle size distribution measurements; a double (probe and image) spherical aberration corrected JEOL ARM 300F operated at 300 keV for high-resolution HAADF imaging (probe convergence semi-angle 26.2 mrad and detector collection semi-angles of 77 to 209 mrad, probe current of 25 pA); and a probe spherical aberration corrected JEOL ARM 200F operated at 200 keV equipped with a dual window EDX detectors (JEOL Centurio) for EDX analysis.

APT

In order to obtain representative APT-ready samples, a 300 nm-thick Ag coating was applied using a stand-alone magnetron sputter source operated at 200 mA with 10 sccm Ar after IGC fabrication and deposition of the Au-Cu nanoparticles onto the flat-top silicon post.[27] The

coating material was selected for being non-refractory, non-oxide forming, for resulting in no overlaps in the APT mass spectrum with the nanoparticle elements, and for having a similar evaporation field to the actual sample material: 24 V/nm for Ag^{1+}, 33 V/nm for Si^{2+}, 30 V/nm for Cu^{1+} and 52 V/nm for Au^{1+}. Moreover, Ag is also relatively ductile, which minimizes the likelihood of sample fracture during APT analysis. Following encapsulation, a Focused Ion Beam (FIB) (Zeiss NVision) was used to produce needle-shaped tips from the Ag-encapsulated Si posts, with a final apex diameter less than 40 nm. Details of the milling conditions are listed in Table 1. The low voltage cleaning was necessary to ensure minimal Ga^{+} implantation in the final sample.[29] All samples were then analyzed in a Cameca LEAP 3000X-HR instrument. A pulsed laser mode (532 nm) was employed with beam energy varied from 0.05 to 0.3 nJ at a 100 kHz pulsing rate. The temperature of the sample stage was set in all analyses to 55K. Each successful analysis typically yielded between 1-3 identified nanoparticles in the resulting APT reconstructions. For the data analysis, IVAS^{TM} 3.6.12 was used. Reconstruction was done in the shank angle mode, with parameter settings best to rebuild the round shape of the embedded particles. Composition analysis is based on the correct identification of ion species. Typical mass spectra are shown in Figure 1. C^{1+}, Si^{2+}, Si^{1+}, H_2O^{1+}, CO_2^{1+}, Cu^{1+}, Ag^{1+}, $AgOH_2^{1+}$ and Au^{1+} ions are identified as the major species. There is no major detection of Ga, meaning that the FIB damage is minimum. Ag^{1+} and $AgOH_2^{1+}$ come from the capping layer. Formation of $AgOH_2^{1+}$ could be attributed to the interaction between the surface of the Ag coating and water vapor. This proves the importance of capping the nanoparticles to protect them from ambient air. C^{1+}, H_2O^{1+} and CO_2^{1+} ions mainly come from contaminations both during the particle fabrication and atom probe analysis. Si^{2+}, Si^{1+}, Cu^{1+} and Au^{1+} are the constituting elements of the post and of the particles, respectively.

Step	Voltage	Current	Time	Profile
1 doughnut shape cutting	30kV	150pA	250 s	Line width 1.8μm, height 5μm
2 annular milling	30kV	10-40pA	Dwelling 1-10μs per pixel	Outer radius 2μm, inner radius 0.1μm
3 low energy cleaning	2kV	10pA	Varies	Light cleaning subject to conditions

Table 1: Parameters used during FIB preparation to mill embedded nanoparticle samples into final APT samples

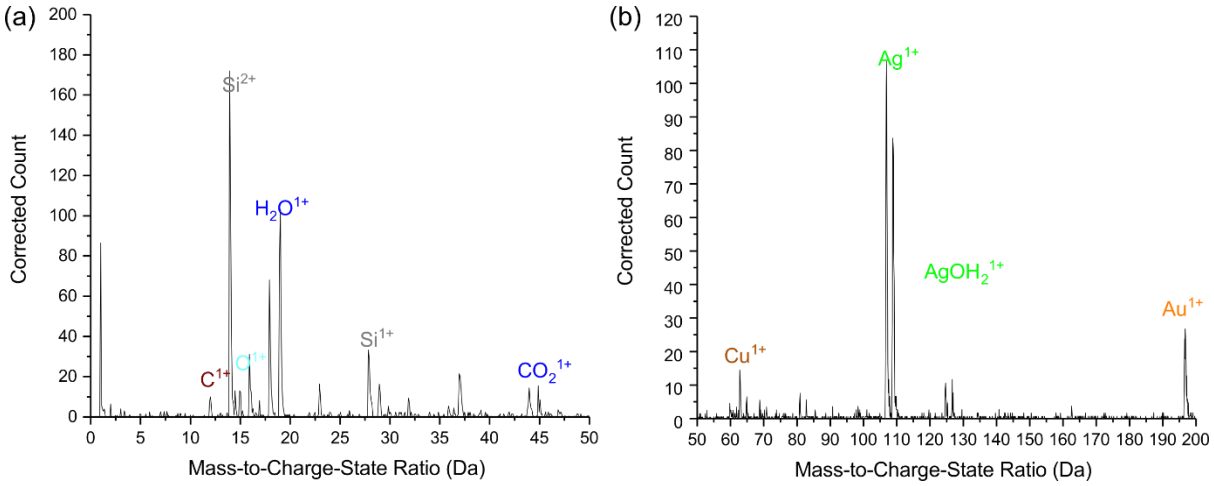

Figure 1 Mass spectra of isolated nanoparticles embedded within the sample produced. a) mass spectrum between Da 0-50 and b) mass spectrum between Da 50-200.

Results and Discussion

Particle fabrication

Recorded size distributions of the ICG-fabricated particles have been deduced from the in-situ mass filter, assuming an alloy density of 14.11 g/cm^3 and a spherical shape (Figure 2a). The distribution is bimodal, and all as-fabricated bimetallic particles display a size below 10 nm according to the above-mentioned hypotheses. Individual Au and Cu signals obtained by operating only one of the individual metal targets under the same conditions were also recorded, and the sum of the two individual signals is shown for comparison. The summation curve would be identical to the curve obtained for binary particles if there was no interaction among the plasmas. By comparing the profile shapes however, two distinct features confirm particle alloying occurs during the fabrication process. The population of smaller particles (named as range A below) is less prominent in the experimental curve than the predicted Au + Cu summation; and, together with a broadening across the overall size distribution, a

secondary maximum (named as range B below) appears in the experimental curve, corresponding to the potentially alloyed particles.

Figure 2b shows a histogram of particle sizes as measured from bright field TEM images (Data obtained from ImageJ with 250 measurements), an example of which is presented in Figure 2c. The TEM analysis in Figure 2b confirms the bimodal nature of the size distribution. Compared with the size distribution extrapolated from in-line mass filtering, the population of smaller particles in range A (2-4 nm) is less prominent and the size distribution in range B (6-12 nm) is broader than was monitored for the as-fabricated particles. Two possible explanations can be given to account for this discrepancy. The first possibility is that collisions occur between small uncharged particles, undetected by the quadrupole mass filter, or between charged and uncharged particles. Since nanoparticles are evenly distributed on the TEM sample substrate, and there is no direct evidence of nanoparticle agglomeration, it is therefore speculated that the coalescence could rather occur after passing through the mass filter and before impacting the grid, shifting the shape of the resulting distribution in favor of larger particles at the expense of the smaller ones. Another possible explanation is linked to the existence of multiply charged particles, which would make one underestimate their size based on m/z measurements. Overall however, both the mass filter and TEM analysis are in good agreement, confirming that two populations of particles are formed by IGC and deposited on the substrate.

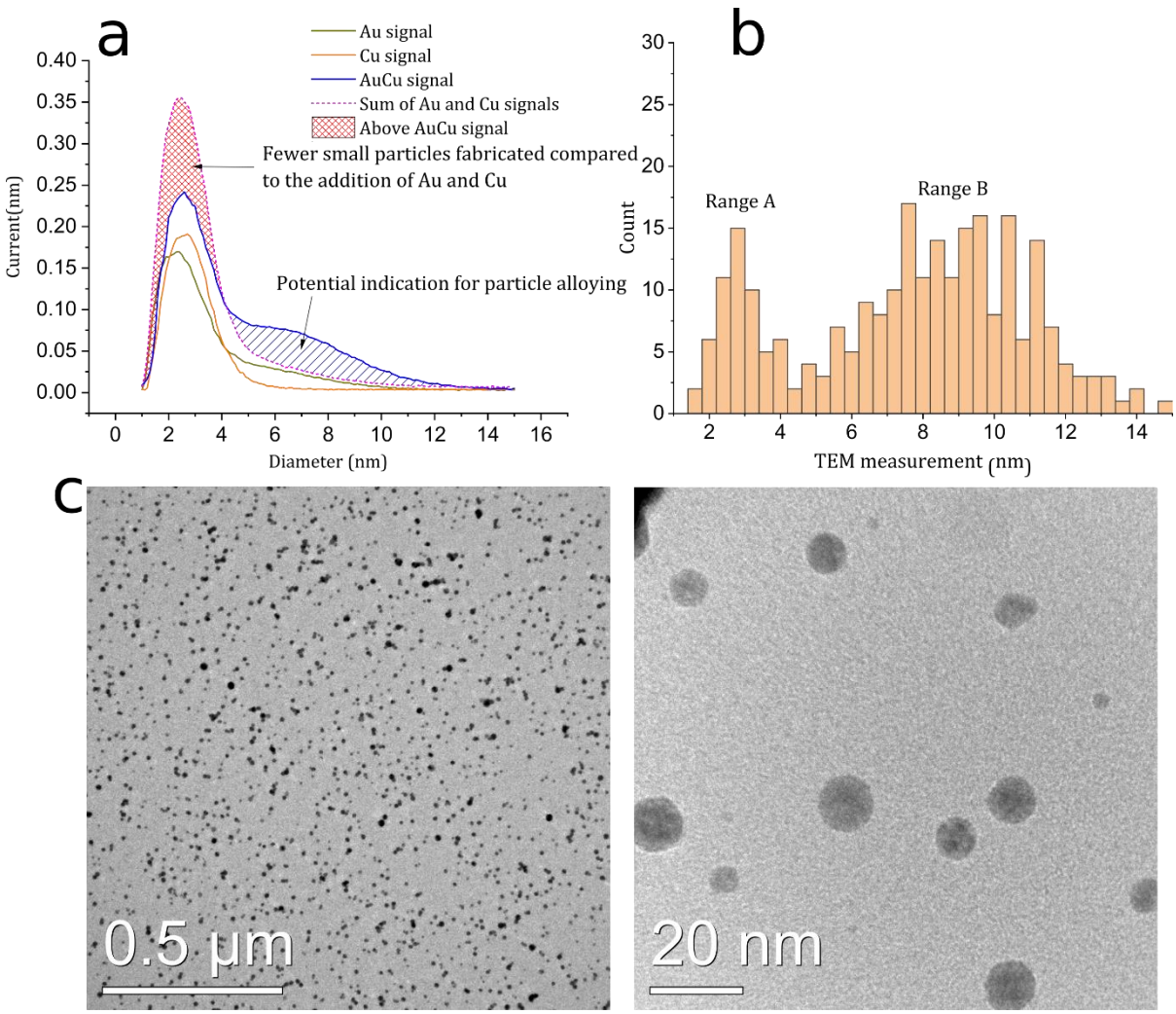

Figure 2 Size distribution of Au-Cu nanoparticles. a) As monitored by the in-line mass filter. The green and yellow lines are the individual Au and Cu deposition measurements, while the solid blue line represents the experimental measurement of the AuCu deposition. Red dashed line represents the summation of individual Au and Cu signals. b) Size distribution measurement based on the TEM images, showing a similar bimodal distribution as per the Meso-Q^{TM} profile. c) Bright field TEM images of the as-deposited Au-Cu nanoparticles on the lacey carbon film. The nanoparticle coverage on the carbon film support is uniform, with no obvious agglomeration observed.

TEM analysis

For pure Au particles, three structures have been identified in prior studies: icosahedron (Ih), decahedron (Dh) and face centered-cubic (fcc)[2]. Figure 3a-f shows Bright Field (BF) and High Angle Annular Dark-Field imaging (HAADF) images of representative Au-Cu particles of different sizes. Both Dh and Ih structures imaged with a 2-fold symmetry are present. Figure 3a

and c show particles belonging to Range B with a Dh structure, while Figure 3b shows the co-existence of Ih and Dh structures at a similar size (D~7 nm).[30,31] For smaller particles (Range A), only the Ih structure is apparent (Figure 3e and f). Particles displaying a Dh structure are thus exclusively present within Range B, while the Ih structure is found across the entire size distribution, in agreement with prior studies on similarly-sized Au nanoparticles.[32–34] The occurrence of the Ih → Dh transition is strongly associated with the particle size.[33,35] The Dh structure is more stable for larger particles, but large Ih particles need to be heated to transform to the Dh structure,[33] which explains the coexistence of the two structures in range B. The Ih structure is more stable for smaller particles (< 6 nm), [33,35] but they are more likely to experience structural transformation to Dh under exposure to an electron beam.[36]

The spatial distribution of Cu atoms within the particles was examined by EDX using a JEOL ARM 200F. Figure 3g shows EDX images of three nanoparticles, in which two are 4nm in diameter and one 10nm. One of the small particles slightly overlaps with the larger one (particle 2 and 3). These three particles all fit within either the Range A or B classification. In terms of chemistry, the EDX data shows that both Cu and Au elements are present within all three individual particles, but with different elemental distributions. To clarify this, Figure 3h shows a schematic illustration of the data from Figure 3g, illustrating the apparent Au shell and Cu core structure of particle 1, the alloyed structure of particle 2, and the Au core and Cu shell of the largest one (particle 3). Particle 2 also contains more Cu than particle 3 although there is no strong evidence for a core-shell structure. However, the limitation of the 2D projection in TEM precludes a more definitive conclusion on the relationship between composition and particle size.

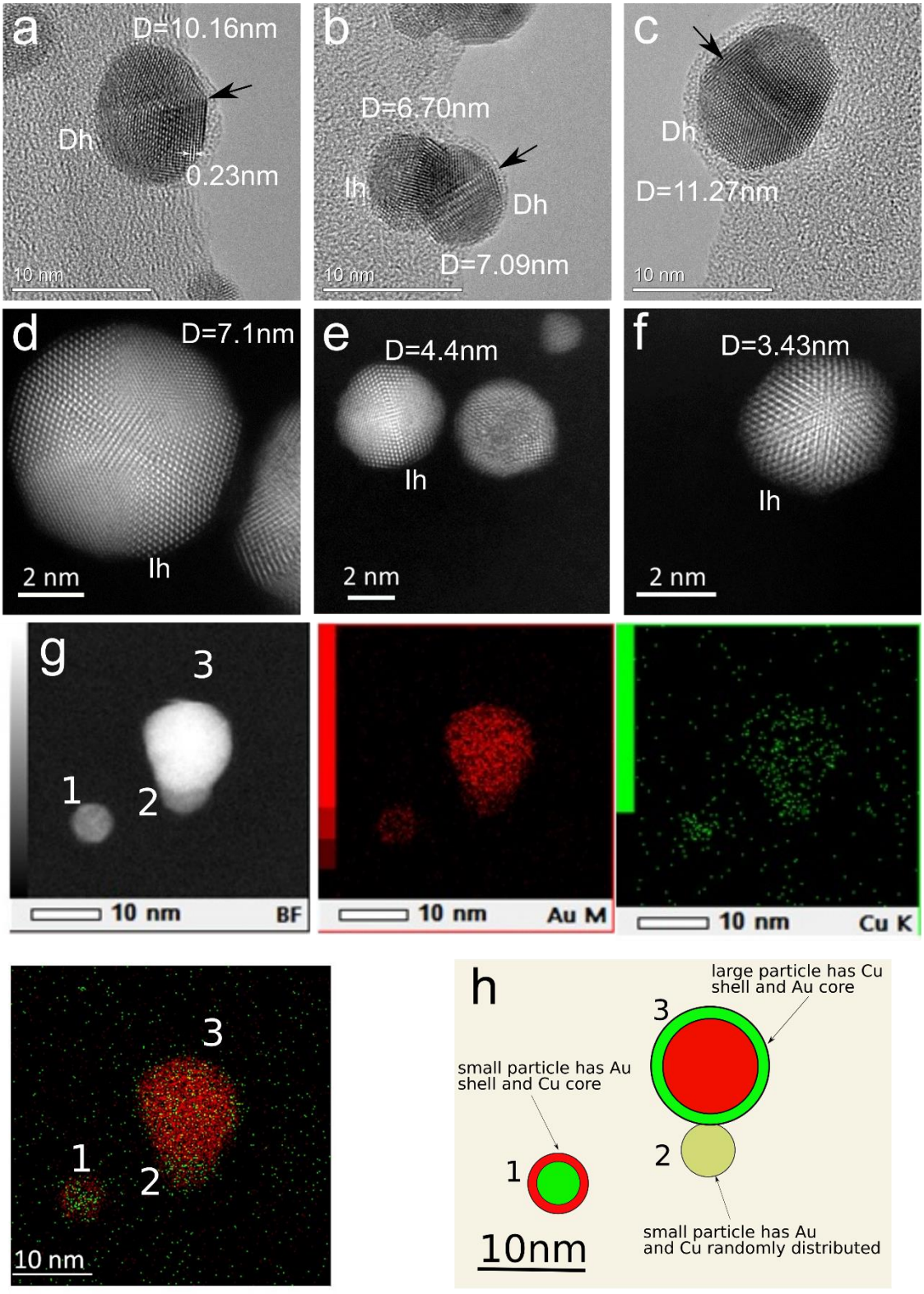

Figure 3 Au-Cu nanoparticles analyzed by 300kV JEOL3000F (a-c) and 300kV ARM 300F Cs corrected TEM (d-f). HAADF images are corrected by rigid alignment. EDX maps on three individual Au-Cu nanoparticles (silicon nitride grid) are shown in (g). The two small particles are labelled as 1 and 2 while the larger nanoparticle is labelled as 3. The scale bar in the EDX scale shows the intensity of received signals. The schematic composition distribution of the particles is shown in (h).

APT

Two APT datasets are presented below, incorporating particles from ranges A and B. It is important to recall that TEM and APT were conducted on particles originating from the same source but deposited on different substrates, suitable for the respective techniques, allowing direct comparison between data. Figure 4a-e shows the typical experiment and data acquisition route. Following deposition of the particles onto the flat-topped doped Si post, an Ag layer was deposited by magnetron sputtering to a thickness of 300 nm. FIB annular milling was then used to produce suitably sharp tips, with around 50 nm of the Ag protective cap remaining at the end of the process (Figure 4e). Figure 4f shows the reconstruction of the APT data, which is in agreement with the structure shown in the schematic inset of Figure 4e, with an Ag capping layer about 10 nm thick. The difference of thickness between SEM and APT measurements derives from the existence of several excessive ion evaporation events when analyzing the Ag layer, which were, later on, filtered out during APT reconstruction via clipping based on the voltage history of the experiment. A sharp interface between the Ag cap and the Si post underneath is present, between which lies a single Au-Cu nanoparticle. This is also shown in Figure 4g, where a 20 at. % Au isoconcentration-surface is used to highlight the nanoparticle for the sake of clarity. The thickness of the Ag layer is less than measured by SEM (~50 nm shown in Figure 4e compared to ~10 nm shown in Figure 4f), most probably due to small bursts of field evaporation during the initial stages of analysis.

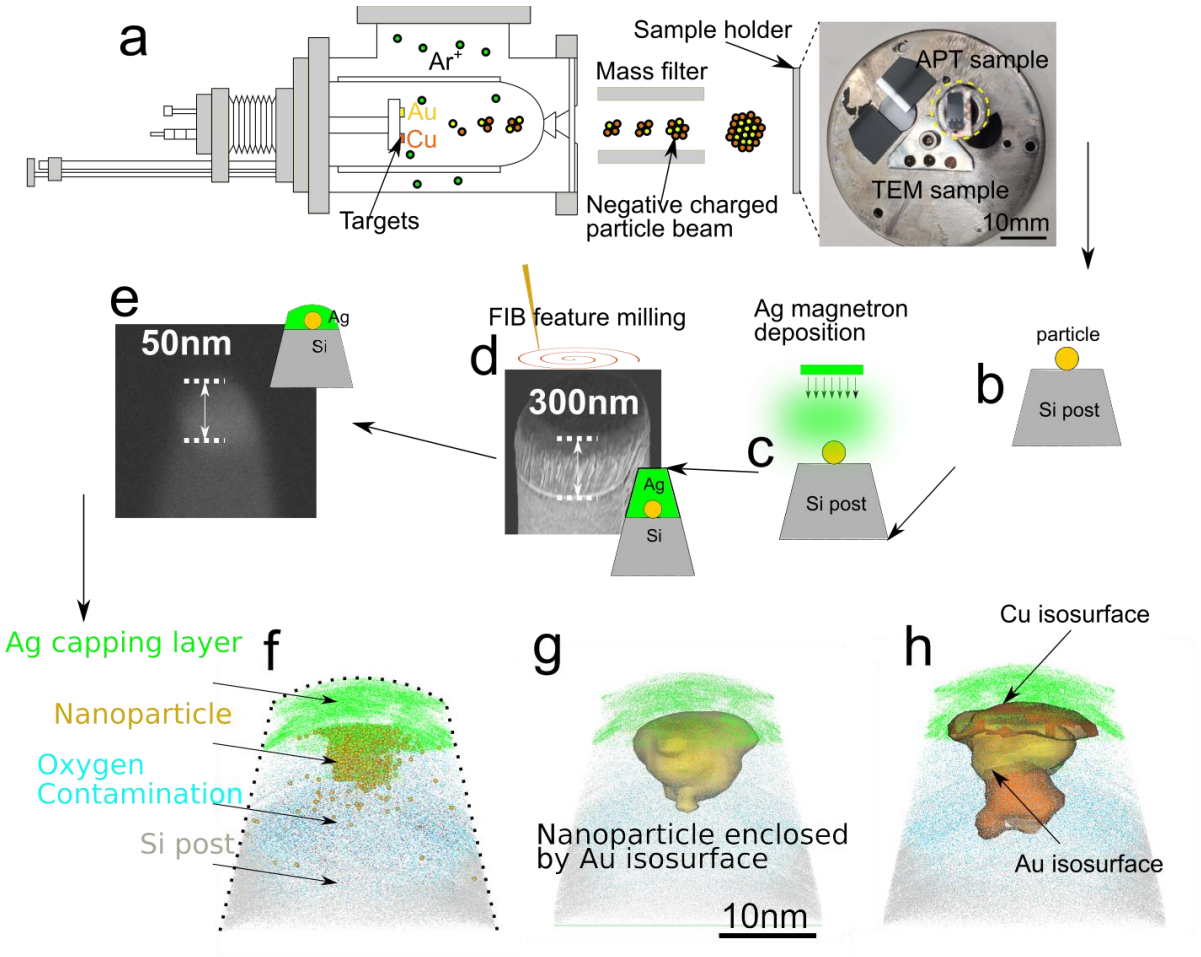

Figure 4 Atom probe experiment and data acquisition procedures. a-b) Particles are fabricated via IGC directly onto a silicon substrate. c) Si flat-top post is capped with 300nm Ag layer. d) FIB then is used to sharpen the tip until 50nm of Ag layer remains. e) SEM image and scheme of a sharpened tip, showing Ag layer (green), Si post (blue) and encapsulated nanoparticle (yellow). f) APT reconstruction of Au-Cu nanoparticle showing that an Ag layer is on the top of the reconstruction, with a fraction blending into the nanoparticle-containing region. Both Au and Cu are detected within the nanoparticle. g) The shape of the tip has been illustrated to reveal the location of various atoms. An (Au 20 at. %) iso-concentration-surface has been applied to highlight the embedded nanoparticle. h) A Cu (Cu 13 at.%) iso-concentration-surface is shown together with Au iso-surface.

In Figure 5, reconstructions of embedded Au-Cu nanoparticles are shown, based on the shank angle protocol,[37] confirming the reproducibility and integrity of the encapsulation process. The particle sizes measured from these datasets are again consistent with a bimodal distribution. Figure 5a-c exhibits three particles within the Range A distribution, whilst Figure 5d-f show a particle belonging to Range B. This classification is based on the calculation of the nominal diameter. For example, for particle labelled 'II' in Figure 5a, the measured volume is 36.9 nm^3, yielding a calculated diameter of 4.1 nm, assuming a perfect sphere. For particle 'IV', the

volume is about 1250 nm^3 with a calculated diameter of 13.4 nm. The compositions of all detected particles in Figure 5 are reported in Table 2.

Table 2: Compositions of the four nanoparticles labelled in Figure 5.

Particle label	I	II	III	IV
C_{Au} (at. %)	88.0	51.7	81.6	63.4
C_{Cu} (at. %)	12.0	48.3	18.4	36.6
Particle diameter (nm)	4.6	4.1	5.8	13.4

In Figure 5a-c, the APT analysis shows three nanoparticles incorporated within a single reconstruction, highlighted using an Au iso-surface of 5 at. %. The reconstructed shapes and sizes are in good agreement with expectations from the mass-filtering and TEM data, although the nanoparticle in the center (particle 'II') has a somewhat compressed shape. This potential reconstruction artefact is likely caused by local preferential evaporation of the encapsulating silver atoms at the matrix-particle interface. The other two nanoparticles have near-spherical shapes although they are only partially captured within the field-of-view. Due to the small sizes of these detected particles, a proximity histogram based on an iso-concentration surface cannot provide suitably accurate compositions. Therefore, to further interpret the distribution of Au and Cu within each particle, 2D concentration projections provided a qualitative examination, as shown in Figure 5b and c. It is apparent from these that Au and Cu are segregated somewhat randomly within these small nanoparticles. In particular, for Range A particles examined by APT, the composition variation is significant: while the Cu content in two of the three detected particles is minimal (12 and 18.4 at. %, respectively), the other is 48.3 at%. The stabilization of Ih small particles despite their exposure to an electron beam, as evidenced by TEM data, may be linked to Cu inclusion detected by APT, which prevents any structural change.

Figure 5d-f presents an individual embedded particle for a more in-depth composition analysis. In this, the uppermost surface in the reconstruction is slightly flattened, possibly due to a mini-fracture during analysis (a process whereby a fraction of material breaks off without ion detection). The figure also appears to show some Ag present within the nanoparticle, which may be caused by diffusion during the Ag deposition process or from an artefact from local magnification effects

in the APT analysis, as seen in other similar nano-sized features.[20,25,38] The calculated diameter, 13.4 nm, is very close to that directly measured from the atom map, confirming accurate reconstruction, and that it lies within the Range B type. Oxygen atoms present are consistent with the known formation of a thin silica layer on top of the silicon microtip. In general, Au and Cu atoms are well embedded within the nanoparticle, with some atoms detected as dispersed elsewhere in the reconstruction volume. This could be due to slight trajectory aberrations, or more likely due to lone atoms/very small nanoparticles laid down during the deposition process.

The distribution of Au and Cu ions through this nanoparticle is examined by proximity histogram and 1D concentration profile, as shown in Figure 5e-f. In Figure 5e, a proximity histogram is defined based on a 20 at% Au iso-surface. From this, Cu surface enrichment is clearly evidenced, reaching an atomic ratio of 1:2 Au:Cu within the first 1 nm of the surface. The Au content gradually increases towards the nanoparticle center, reaching a ratio of 5:1. 1D concentration profiles applied to the same nanoparticle are shown in Figure 5f. By applying this analysis both to parallel and perpendicular directions of evaporation in the APT, any possible artefacts from preferential evaporation along the analysis direction (z-direction) are identified. In both orientations, the 1D concentration profiles show that the distributions of Au and Cu are inhomogeneous, and do not fundamentally differ. The Au-core/Cu-shell structure identified is in agreement with the structure seen in the Range B particles analyzed by TEM-EDX.

Combining the three types of data (mass filtering, TEM and APT), it is now possible to draw a much more detailed picture of the diversity of particles formed by IGC deposition. A Cu enrichment on the surface of the larger particles (range B) has been indicated by both TEM and APT, and a precise, quantitative composition profile within the Cu-enriched shell can be obtained by APT, consistent regardless of the direction of analysis. For the Range A particles detected by APT, the elemental composition is much less ordered with no distinct segregation but with significant variations of composition between the neighboring particles. Moreover, HR-TEM has shown that, though the Ih structure presents a higher energy compared to the Dh structure, Ih is the dominant structure for Range A particles. It may be deduced from the APT results that alloying Cu into an Au particle smaller than 4 nm stabilizes the Ih structure.

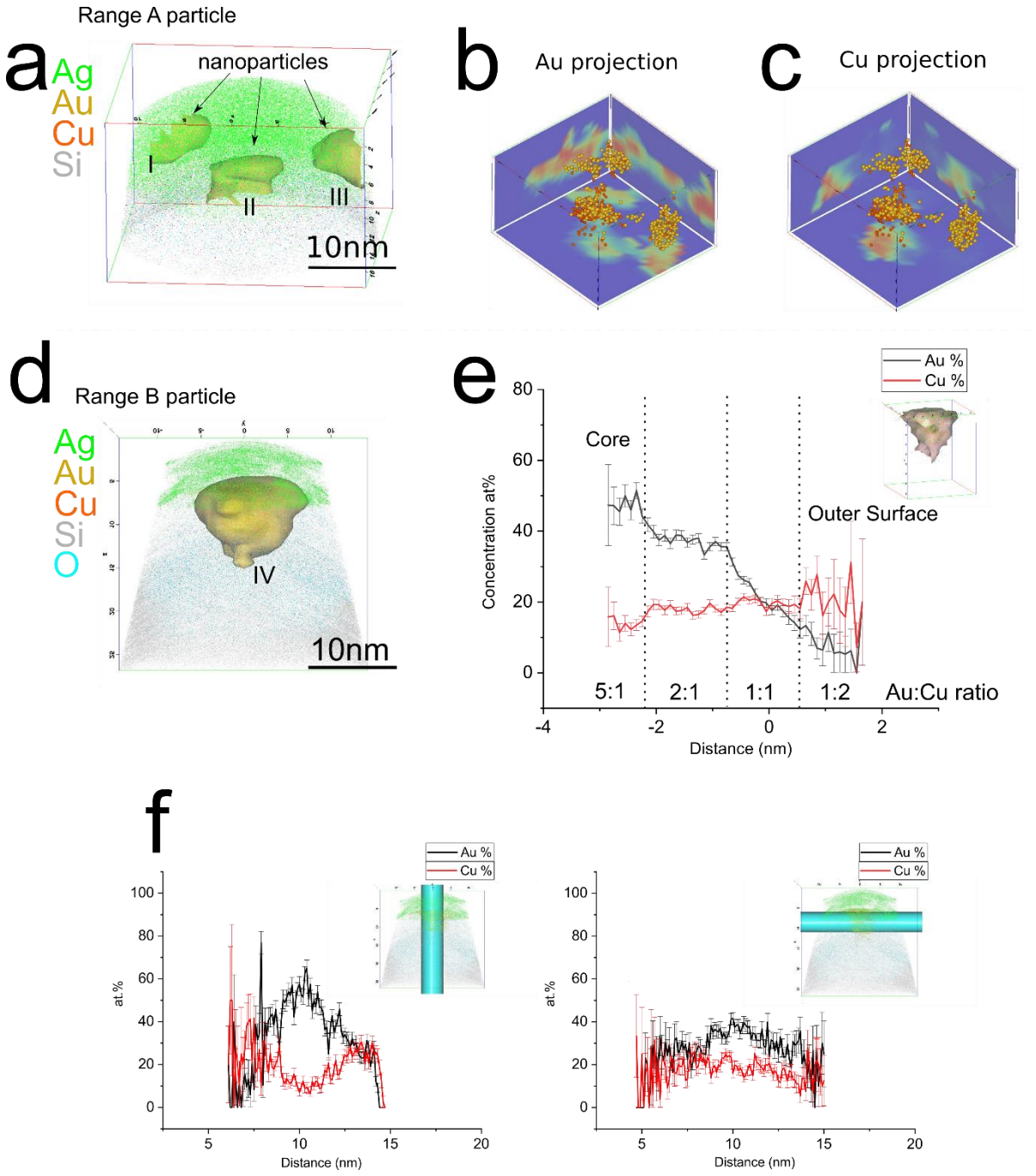

Figure 5 APT analysis for a-c) three Range A particles and d-f) a single Range B particle. a) 3 particles identified within atom map, b), c) 2D contour distribution of Au and Cu ions. Red color represents high concentration of analyzed element. Green color means low concentration. d) Individual particle embedded in the center of the reconstruction. e) Au and Cu distribution derived from proximity histogram based on 20 at% Au iso-surface. f) Au and Cu distribution derived from 1D concentration analyses parallel and perpendicular to the analysis direction.

Conclusion

In summary, inert gas condensation (IGC) procedures lead to the formation of metastable Au-Cu bimetallic nanoparticles, with comparatively tight size distributions but with variations in microstructural shapes and composition. By applying IGC to the deposition of Au-Cu nanoparticles onto two different substrates, a TEM grid and a flat-top Si coupon for APT analysis, we have demonstrated that the combination of the two analysis techniques allow one to investigate complex, multi-metallic nanoparticles and/or specific geometrical shapes/structures. TEM data provide evidence that Au-Cu bimetallic particles are produced in out-of-equilibrium states and coexist with various shapes and structures. However, the composition maps given by TEM-EDX analysis are mostly qualitative, and the 3D distribution of the two elements within Au-Cu nanoparticles is revealed at a deeper atomic scale by APT. The APT data provide in depth information on the composition of the nanoparticles. Cu as an alloying element acts to stabilize the Ih structure for particles smaller than 4 nm, while there is indication that Cu may segregate to the surface of particles larger than 10 nm. If expanded to other multimetallic systems, this dual characterization strategy has significant potential for investigating the advantages and the limits of the IGC method, as it provides quantitative information on the relationship between the size, the structure and the composition of the particles, and on the variability of these characteristics.

Acknowledgements

Qifeng Yang gives thanks to Dr Daniel Haley and Dr Andrew London for the use of atom probe data analysis tools (https://sourceforge.net/projects/atomprobelab/, http://threedepict.sourceforge.net/). The LEAP 3000 was funded by EPSRC under grant EP/D077664/1. This work has benefited from the support of the French National Research Agency (ANR), through the NobleFreeCat project (ANR-17-CE07-0022), and from the BQRI program from Université de Lille. Chevreul Institute (FR 2638), Ministère de l'Enseignement Supérieur et de la Recherche, Région Hauts-de-France and FEDER are acknowledged for supporting this work.

References

(1) Vajda, S.; White, M. G. Catalysis Applications of Size-Selected Cluster Deposition. *ACS Catal.* **2015**, *5*, 7152–7176.

(2) Plant, S. R.; Cao, L.; Palmer, R. E. Atomic Structure Control of Size-Selected Gold Nanoclusters during Formation. *J. Am. Chem. Soc.* **2014**, *136*, 7559–7562.

(3) Gracia-Pinilla, M.; Martínez, E.; Vidaurri, G. S.; Pérez-Tijerina, E. Deposition of Size-Selected Cu Nanoparticles by Inert Gas Condensation. *Nanoscale Res. Lett.* **2010**, *5*, 180–188.

(4) Yin, F.; Wang, Z. W.; Palmer, R. E. Controlled Formation of Mass-Selected Cu–Au Core–Shell Cluster Beams. *J. Am. Chem. Soc.* **2011**, *133*, 10325–10327.

(5) Pérez-Tijerina, E.; Gracia Pinilla, M.; Mejía-Rosales, S.; Ortiz-Méndez, U.; Torres, A.; José-Yacamán, M. Highly Size-Controlled Synthesis of Au/Pd Nanoparticles by Inert-Gas Condensation. *Faraday Discuss.* **2008**, *138*, 353–362.

(6) Cassidy, C.; Singh, V.; Grammatikopoulos, P.; Djurabekova, F.; Nordlund, K.; Sowwan, M. Inoculation of Silicon Nanoparticles with Silver Atoms. *Sci. Rep.* **2013**, *3*, 3083.

(7) Krishnan, G.; Verheijen, M. A.; Ten Brink, G. H.; Palasantzas, G.; Kooi, B. J. Tuning Structural Motifs and Alloying of Bulk Immiscible Mo-Cu Bimetallic Nanoparticles by Gas-Phase Synthesis. *Nanoscale* **2013**, *5*, 5375–5383.

(8) Johnson, G. E.; Colby, R.; Engelhard, M.; Moon, D.; Laskin, J. Soft Landing of Bare PtRu Nanoparticles for Electrochemical Reduction of Oxygen. *Nanoscale* **2015**, *7*, 12379–12391.

(9) Holse, C.; Elkjær, C. F.; Nierhoff, A.; Sehested, J.; Chorkendorff, I.; Helveg, S.; Nielsen, J. H. Dynamic Behavior of CuZn Nanoparticles under Oxidizing and Reducing Conditions. *J. Phys. Chem. C* **2015**, *119*, 2804–2812.

(10) Singh, V.; Cassidy, C.; Grammatikopoulos, P.; Djurabekova, F.; Nordlund, K.; Sowwan, M. Heterogeneous Gas-Phase Synthesis and Molecular Dynamics Modeling of Janus and Core-Satellite Si-Ag Nanoparticles. *J. Phys. Chem. C* **2014**, *118*, 13869–13875.

(11) Caillard, A.; Cuynet, S.; Lecas, T.; Andreazza, P.; Mikikian, M.; Thomann, A. L.; Brault, P. PdPt Catalyst Synthesized Using a Gas Aggregation Source and Magnetron Sputtering for Fuel Cell Electrodes. *J. Phys. D. Appl. Phys.* **2015**, *48*.

(12) Krishnan, G.; De Graaf, S.; Ten Brink, G. H.; Persson, P. O. Å.; Kooi, B. J.; Palasantzas, G. Strategies to Initiate and Control the Nucleation Behavior of Bimetallic Nanoparticles. *Nanoscale* **2017**, *9*, 8149–8156.

(13) Bohra, M.; Grammatikopoulos, P.; Singh, V.; Zhao, J.; Toulkeridou, E.; Steinhauer, S.; Kioseoglou, J.; Bobo, J. F.; Nordlund, K.; Djurabekova, F.; *et al.* Tuning the Onset of Ferromagnetism in Heterogeneous Bimetallic Nanoparticles by Gas Phase Doping. *Phys. Rev. Mater.* **2017**, *1*, 1–12.

(14) Pérez-Tijerina, E.; Mejía-Rosales, S.; Inada, H.; José-Yacamán, M. Effect of Temperature on AuPd Nanoparticles Produced by Inert Gas Condensation. *J. Phys. Chem. C* **2010**, *114*, 6999–7003.

(15) Mayoral, A.; Mejía-Rosales, S.; Mariscal, M. M.; Pérez-Tijerina, E.; José-Yacamán, M. The Co-Au Interface in Bimetallic Nanoparticles: A High Resolution STEM Study. *Nanoscale* **2010**, *2*, 2647–2651.

(16) MacArthur, K. E.; Slater, T. J. A.; Haigh, S. J.; Ozkaya, D.; Nellist, P. D.; Lozano-Perez, S. Quantitative Energy-Dispersive X-Ray Analysis of Catalyst Nanoparticles Using a Partial Cross Section Approach. *Microsc. Microanal.* **2016**, *22*, 71–81.

(17) Batenburg, K. J.; Bals, S.; Sijbers, J.; Kübel, C.; Midgley, P. A.; Hernandez, J. C.; Kaiser, U.; Encina, E. R.; Coronado, E. A.; Van Tendeloo, G. 3D Imaging of Nanomaterials by Discrete Tomography. *Ultramicroscopy* **2009**, *109*, 730–740.

(18) Gault, B.; Moody, M. P.; Cairney, J. M.; Ringer, S. P. *Atom Probe Microscopy*; Springer Science & Business Media, 2012.

(19) Tedsree, K.; Li, T.; Jones, S.; Chan, C. W. A.; Yu, K. M. K.; Bagot, P. A. J.; Marquis, E. A.; Smith, G. D. W.; Tsang, S. C. E. Hydrogen Production from Formic Acid

Decomposition at Room Temperature Using a Ag-Pd Core-Shell Nanocatalyst. *Nat. Nanotechnol.* **2011**, *6*, 302–307.
(20) Li, T.; Bagot, P. A. J.; Christian, E.; Theobald, B. R. C.; Sharman, J. D. B.; Ozkaya, D.; Moody, M. P.; Tsang, S. C. E.; Smith, G. D. W. Atomic Imaging of Carbon-Supported Pt, Pt/Co, and Ir@Pt Nanocatalysts by Atom-Probe Tomography. *ACS Catal.* **2014**, *4*, 695–702.
(21) Eley, C.; Li, T.; Liao, F.; Fairclough, S. M.; Smith, J. M.; Smith, G.; Tsang, S. C. E. Nanojunction-Mediated Photocatalytic Enhancement in Heterostructured CdS/ZnO, CdSe/ZnO, and CdTe/ZnO Nanocrystals. *Angew. Chem. Int. Ed. Engl.* **2014**, *53*, 7838–7842.
(22) Waugh, A. R.; Boyes, E. D.; Southon, M. J. Investigations of Field Evaporation with a Field-Desorption Microscope. *Surf. Sci.* **1976**, *61*, 109–142.
(23) Felfer, P.; Benndorf, P.; Masters, A.; Maschmeyer, T.; Cairney, J. M. Revealing the Distribution of the Atoms within Individual Bimetallic Catalyst Nanoparticles. *Angew. Chemie Int. Ed.* **2014**, *53*, 11190–11193.
(24) Felfer, P.; Li, T.; Eder, K.; Galinski, H.; Magyar, A.; Bell, D.; Smith, G. D. W.; Kruse, N.; Ringer, S. P.; Cairney, J. M. New Approaches to Nanoparticle Sample Fabrication for Atom Probe Tomography. *Ultramicroscopy* **2015**.
(25) Larson, D. J. J.; Giddings, A. D. D.; Wu, Y.; Verheijen, M. A. A.; Prosa, T. J. J.; Roozeboom, F.; Rice, K. P. P.; Kessels, W. M. M. M. M.; Geiser, B. P. P.; Kelly, T. F. F. Encapsulation Method for Atom Probe Tomography Analysis of Nanoparticles. *Ultramicroscopy* **2015**, *159*, 420–426.
(26) Folcke, E.; Lardé, R.; Le Breton, J. M.; Gruber, M.; Vurpillot, F.; Shield, J. E.; Rui, X.; Patterson, M. M. Laser-Assisted Atom Probe Tomography Investigation of Magnetic FePt Nanoclusters: First Experiments. *J. Alloys Compd.* **2012**, *517*, 40–44.
(27) Yang, Q.; Joyce, D. E.; Saranu, S.; Hughes, G. M.; Varambhia, A.; Moody, M. P.; Bagot, P. A. J. A Combined Approach for Deposition and Characterization of Atomically Engineered Catalyst Nanoparticles. *Catal. Struct. React.* **2015**, *1*, 125–131.
(28) Kusior, A.; Kollbek, K.; Kowalski, K.; Borysiewicz, M.; Wojciechowski, T.; Adamczyk, A.; Trenczek-Zajac, A.; Radecka, M.; Zakrzewska, K. Sn and Cu Oxide Nanoparticles Deposited on TiO2 Nanoflower 3D Substrates by Inert Gas Condensation Technique. *Appl. Surf. Sci.* **2016**, 1–10.
(29) Douglas, J. O.; Bagot, P. A. J.; Johnson, B. C.; Jamieson, D. N.; Moody, M. P. Optimisation of Sample Preparation and Analysis Conditions for Atom Probe Tomography Characterisation of Low Concentration Surface Species. *Semicond. Sci. Technol.* **2016**, *31*, 084004.
(30) Reyes-Gasga, J.; Tehuacanero-Nuñez, S.; Montejano-Carrizales, J. M.; Gao, X.; Jose-Yacaman, M. Analysis of the Contrast in Icosahedral Gold Nanoparticles. *Top. Catal.* **2007**, *46*, 23–30.
(31) Casillas, G.; Palomares-Báez, J.; Rodríguez-López, J.; Luo, J.; Ponce, A.; Esparza, R.; Jesúsvelázquez-Salazar, J.; Hurtado-Macias, A.; González-Hernández, J.; José-Yacaman, M. In Situ Tem Study of Mechanical Behaviour of Twinned Nanoparticles. *Philos. Mag.* **2012**, *92*, 4437–4453.
(32) Young, N. P.; van Huis, M. A.; Zandbergen, H. W.; Xu, H.; Kirkland, A. I. Transformations of Gold Nanoparticles Investigated Using Variable Temperature High-Resolution Transmission Electron Microscopy. *Ultramicroscopy* **2010**, *110*, 506–516.
(33) Barnard, A. S.; Young, N. P.; Kirkland, A. I.; van Huis, M. A.; Xu, H. Nanogold: A Quantitative Phase Map. *ACS Nano* **2009**, *3*, 1431–1436.
(34) Li, Z. Y.; Young, N. P.; Di Vece, M.; Palomba, S.; Palmer, R. E.; Bleloch, a L.; Curley, B. C.; Johnston, R. L.; Jiang, J.; Yuan, J. Three-Dimensional Atomic-Scale Structure of Size-Selected Gold Nanoclusters. *Nature* **2008**, *451*, 46–48.
(35) Huang, R.; Wen, Y. H.; Shao, G. F.; Zhu, Z. Z.; Sun, S. G. Single-Crystalline and Multiple-Twinned Gold Nanoparticles: An Atomistic Perspective on Structural and Thermal Stabilities. *RSC Adv.* **2014**, *4*, 7528–7537.
(36) Wang, Z. W.; Palmer, R. E. Determination of the Ground-State Atomic Structures of Size-Selected Au Nanoclusters by Electron-Beam-Induced Transformation. *Phys. Rev. Lett.* **2012**, *108*, 1–5.
(37) Gault, B.; Haley, D.; de Geuser, F.; Moody, M. P.; Marquis, E. A.; Larson, D. J.; Geiser,

B. P. Advances in the Reconstruction of Atom Probe Tomography Data. *Ultramicroscopy* **2011**, *111*, 448–457.

(38) London, A. J.; Lozano-Perez, S.; Moody, M. P.; Amirthapandian, S.; Panigrahi, B. K.; Sundar, C. S.; Grovenor, C. R. M. Quantification of Oxide Particle Composition in Model Oxide Dispersion Strengthened Steel Alloys. *Ultramicroscopy* **2015**.